

Graphene coated subwavelength wires: A theoretical investigation of the emission and radiation properties

Mauro Cuevas

Consejo Nacional de Investigaciones Científicas y Técnicas (CONICET) and Facultad de Ingeniería y Tecnología Informática, Universidad de Belgrano, Villanueva 1324, C1426BMJ, Buenos Aires, Argentina
Grupo de Electromagnetismo Aplicado, Departamento de Física, FCEN, Universidad de Buenos Aires, Ciudad Universitaria, Pabellón I, C1428EHA, Buenos Aires, Argentina

E-mail: cuevas@df.uba.ar

Abstract. This work analyzes the emission and radiation properties of a single optical emitter embedded in a graphene-coated subwavelength wire. We discuss the modifications of the spontaneous emission rate and the radiation efficiency as a function of the position and orientation of the dipole inside the wire. Our results show that these quantities can be enhanced by several orders of magnitude when the emission frequency coincides with one of the resonance frequencies of the graphene-coated wire. In particular, high-order plasmon resonances are excited when the emitter is moved from the wire center. The modifications by varying the orientation of the dipole in the near field distribution and in the far field intensities are shown.

PACS numbers: 81.05.ue,73.20.Mf,78.68.+m,42.50.Pq

Keywords: graphene, surface plasmons, quantum electrodynamics, plasmonics

1. Introduction

Surface plasmon polariton results from the coherent coupling of photons to surface charge density oscillations [1, 2]. In natural plasmonic materials such as metals, constitutive parameters such as the conductivity and charge density are fixed, whereas they can be tuned in graphene electrically or by chemical doping [3], which has a dramatic effect on its optical properties. As the linear band structure of graphene causes the plasmon mass to depend on the Fermi-level position, electrically tunable surface plasmons can be supported by graphene from microwaves to the mid-infrared regimes [4]. This has aroused new interest in studying graphene in the context of optical and plasmonic applications, including graphene quantum dots as a new generation of light-emitting devices [5], sensing [6], solar cells [7], to mention just a few.

Surface plasmons polaritons can be roughly divided into two categories: surface plasmon (SPs) propagating along waveguiding structures, such as an infinite flat graphene monolayer, and localized surface plasmons (LSPs) supported by spatially limited structures, such as scattering particles. Both kind of plasmon modes can be excited when a single optical emitter (such as quantum dots and single molecules) is placed next to one of the aforementioned structures. As a result of the high light confinement, an enhanced decay rate of the emitter into the plasmonic mode via the Purcell effect take place [8]. In fact, it was recently showed that the interplay between an optical emitter and a graphene-coated sphere leads to an enhancement of the spontaneous emission into confined plasmonic modes [9]. A variety of structures such as infinite graphene monolayers [10, 11, 12, 13], ribbons or nanometer sized disks [14] and double graphene waveguides [15, 16] have been the object of intensive research over the last few years due to the possibility to engineer surface plasmon mode density of states to control emission properties.

In this paper we consider a cylindrical dielectric core coated with a graphene layer and we investigate the role of the LSPs in modifying the emission and radiation rates of an emitter placed inside the graphene-coated cylinder. In this context, several works focused on the influence that the eigenmodes play on circular dielectric and metallic waveguides [17, 18, 19] or on single wall carbon nanotubes [20]. Such systems offer a new tool for the interplay between

light and matter at the nanometer scale [21, 22]. Other works have presented two dimensional calculations that extend such studies to examining the role of the shape of the waveguide [23, 24]. Two dimensional setting has important properties that allow to understand better the three dimensional case [17, 28], since qualitatively similar trends will hold in three dimensions [24]. Experimental advances in the fabrication of microstructures based on insulating materials such as SiO₂ doped with molecular ions [25], the possibility of encapsulate single atom, molecules and compounds into graphene wires [26] and the fact that thanks to the van der Waals force, a graphene sheet can be tightly coated on a fiber surface [27], encourages an investigation about the emission and radiation characteristics of such graphene based systems.

The paper is organized as follows. First, in Section 2 we sketch an analytical method based on the separation of variables approach and obtain a solution for the electromagnetic field scattered by a graphene-coated wire when an oscillating line dipole source is located at an arbitrary position inside the wire cylinder. We derive analytical expressions for the power emitted and radiated by the source. In section 3 we present examples of emission and radiation decay rates corresponding to wires tightly coated with a graphene layer and compared the results with those obtained in the absence of the graphene coating. Finally, concluding remarks are provided in Section 4. The Gaussian system of units is used and an $\exp(-i\omega t)$ time-dependence is implicit throughout the paper, with ω as the angular frequency, t as the time, and $i = \sqrt{-1}$. The symbols Re and Im are used for denoting the real and imaginary parts of a complex quantity, respectively.

2. Theory

We consider a graphene coated cylinder with circular cross section (radius a) centered at $x = 0$, $y = 0$ (figure 1). The wire substrate is characterized by the electric permittivity ε_1 and the magnetic permeability μ_1 . The coated wire is embedded in a transparent medium with electric permittivity ε_2 and magnetic permeability μ_2 . The graphene layer is considered as an infinitesimally thin, local and isotropic two-sided layer with frequency-dependent surface conductivity $\sigma(\omega)$ given by the Kubo formula [29, 30], which can be read as $\sigma = \sigma^{intra} + \sigma^{inter}$, with the intraband and

interband contributions being

$$\sigma^{intra}(\omega) = \frac{2ie^2k_B T}{\pi\hbar(\omega + i\gamma_c)} \ln [2\cosh(\mu_c/2k_B T)], \quad (1)$$

$$\sigma^{inter}(\omega) = \frac{e^2}{\hbar} \left\{ \frac{1}{2} + \frac{1}{\pi} \arctan [(\omega - 2\mu_c)/2k_B T] - \frac{i}{2\pi} \ln \left[\frac{(\omega + 2\mu_c)^2}{(\omega - 2\mu_c)^2 + (2k_B T)^2} \right] \right\}, \quad (2)$$

where μ_c is the chemical potential (controlled with the help of a gate voltage), γ_c the carriers scattering rate, e the electron charge, k_B the Boltzmann constant and \hbar the reduced Planck constant. The intraband contribution dominates for large doping $\mu_c \ll k_B T$ and is a generalization of the Drude model for the case of arbitrary band structure, whereas the interband contribution dominates for large frequencies $\hbar\omega \geq \mu_c$. A line dipole source (whose axis lie along the \hat{z} axis) with a dipole moment $\vec{p} = p(\cos\alpha\hat{x} + \sin\alpha\hat{y})$ is placed inside the cylinder, at position $\vec{r}' = \rho'\hat{r} + \phi'\hat{\phi}$ ($\rho' < a$). The dipole is aligned at an angle α with respect to the \hat{x} axis, as indicated in figure 1. The current density of the electric dipole is

$$\vec{j}(\vec{r}) = -i\omega\vec{p}\delta(\vec{r} - \vec{r}') = -i\omega\vec{p}\frac{1}{\rho}\delta(\rho - \rho')\delta(\phi - \phi'). \quad (3)$$

In an unbounded medium, the dipole fields are obtained from the vector potential \vec{A} (refer to appendix for its derivation),

$$\vec{A}(\rho, \phi) = \sum_{m=-\infty}^{+\infty} \pi k_0 J_m(k_1 \rho_{<}) H_m^{(1)}(k_1 \rho_{>}) e^{im(\phi - \phi')} \quad (4)$$

$$\times [p_\rho \hat{r} + p_\phi \hat{\phi}],$$

$$\vec{H}(\rho, \phi) = \nabla \times \vec{A} = \hat{z}\varphi(\rho, \phi), \quad (5)$$

$$\vec{E}(\rho, \phi) = \frac{i}{k_0 \varepsilon_1} \nabla \times \vec{H}(\rho, \phi) = -\frac{i}{k_0 \varepsilon_1} \hat{z} \times \nabla_t \varphi, \quad (6)$$

where $\varphi(\rho, \phi)$ is the non-zero component of the total magnetic field along the axis of the wire (\hat{z} axis), $\nabla_t = \hat{r}\frac{\partial}{\partial\rho} + \hat{\phi}\frac{1}{\rho}\frac{\partial}{\partial\phi}$ is the transverse part of the ∇ operator, $k_0 = \omega/c$ is the modulus of the photon wave vector in vacuum, ω is the angular frequency, c is the vacuum speed of light, $\rho_{<} (\rho_{>})$ is the smaller (larger) of ρ and ρ' , p_ρ and p_ϕ are the projection of vector \vec{p} on the \hat{r} and $\hat{\phi}$ axis, respectively, and J_m and $H_m^{(1)}$ are the n th Bessel and Hankel functions of the first kind, respectively. From Eqs. (4) and (5), we obtain the primary magnetic field emitted by the dipole,

$$\varphi_i(\rho, \phi) = \sum_{m=-\infty}^{+\infty} \pi k_0 k_1 J_m(k_1 \rho')$$

$$\times \left[H_m^{(1)'}(k_1 \rho) p_\theta - im \frac{H_m^{(1)}(k_1 \rho)}{k_1 \rho} p_\rho \right] e^{im(\phi - \phi')}, \quad (7)$$

for $\rho > \rho'$, and

$$\varphi_i(\rho, \phi) = \sum_{m=-\infty}^{+\infty} \pi k_0 k_1 H_m^{(1)}(k_1 \rho')$$

$$\times \left[J_m'(k_1 \rho) p_\theta - im \frac{J_m(k_1 \rho)}{k_1 \rho} p_\rho \right] e^{im(\phi - \phi')}, \quad (8)$$

for $\rho < \rho'$.

When the dipole is located inside the coated wire cylinder, the scattered magnetic field along the axis of the wire, *i.e.*, the \hat{z} component, denoted by $\varphi_s^{(j)}$ ($j = 1, 2$), are expanded as a series of cylindrical harmonics, one for the internal region ($\rho < a$, superscript 1) and another one for the external region ($\rho > a$, superscript 2),

$$\varphi_s^{(1)}(\rho, \phi) = \sum_{m=-\infty}^{+\infty} a_m J_m(k_1 \rho) e^{im\phi}, \quad (9)$$

$$\varphi_s^{(2)}(\rho, \phi) = \sum_{m=-\infty}^{+\infty} b_m H_m^{(1)}(k_2 \rho) e^{im\phi}, \quad (10)$$

where a_m and b_m are unknown complex coefficients. Taking into account that because of the graphene coating the tangential components of the magnetic field are no longer continuous across the boundary – as they were in the case of uncoated cylinders – the boundary conditions for our case can be expressed as

$$\frac{1}{\varepsilon_1} \frac{\partial}{\partial\rho} (\varphi_i + \varphi_s^{(1)})|_{\rho=a} = \frac{1}{\varepsilon_2} \frac{\partial}{\partial\rho} \varphi_s^{(2)}|_{\rho=a}, \quad (11)$$

and

$$\varphi_s^{(2)}|_{\rho=a} - (\varphi_i + \varphi_s^{(1)})|_{\rho=a} = \quad (12)$$

$$\frac{4\pi\sigma}{ck_0\varepsilon_1} i \frac{\partial}{\partial\rho} (\varphi_i + \varphi_s^{(1)})|_{\rho=a}.$$

Inserting the expressions (9), (10) and (7) into the boundary conditions, we obtain the amplitudes of the scattered fields,

$$a_m = \frac{\pi k_0}{2iaJ_m(x_1)D_m} \quad (13)$$

$$\times [k_1 a A_m h_m(x_2) + \frac{4\pi\sigma}{c} i k_0 a h_m(x_2) B_m - B_m],$$

$$b_m = \frac{\pi k_0}{2iaH_m^{(1)}(x_2)D_m} [k_1 a A_m j_m(x_1) - B_m], \quad (14)$$

where

$$D_m = h_m(x_2) - j_m(x_1) + \frac{4\pi\sigma}{c} i k_0 a j_m(x_1) h_m(x_2), \quad (15)$$

$$j_m(x_1) = \frac{J_m'(x_1)}{x_1 J_m(x_1)}, \quad (16)$$

$$h_m(x_1) = \frac{H_m^{(1)'}(x_2)}{x_2 H_m^{(1)}(x_2)}, \quad (17)$$

$$A_m = p[J_{m-1}(k_1\rho')f_{m-1}(x_1)e^{i[\phi'-\alpha]} - J_{m+1}(k_1\rho')g_{m+1}(x_1)e^{-i[\phi'-\alpha]}]e^{-im\phi'} \quad (18)$$

$$B_m = \frac{\partial}{\partial x_1} A_m = \quad (19)$$

$$p[J_{m-1}(k_1\rho')f'_{m-1}(x_1)e^{i[\phi'-\alpha]} - J_{m+1}(k_1\rho')g'_{m+1}(x_1)e^{-i[\phi'-\alpha]}]e^{-im\phi'}, \quad (20)$$

$$f_m(x_1) = H_m^{(1)'}(x_1) - m \frac{H_m^{(1)}(x_1)}{x_1}, \quad (21)$$

$$g_m(x_1) = H_m^{(1)'}(x_1) + m \frac{H_m^{(1)}(x_1)}{x_1}$$

and $x_1 = k_1 a$, $x_2 = k_2 a$. Here, the prime denotes the derivative with respect to the argument. The denominator D_m in Eqs. (13) and (14) are the same as that of the Mie scattering coefficients and may become very small in magnitude when the emission frequency coincides with one of the resonance frequencies [31, 32].

In the limit of $\rho' \rightarrow 0$, $A_m = H_m^{(1)'} p(e^{-i\alpha}\delta_{m,1} - e^{i\alpha}\delta_{m,-1})$, $B_m = H_m^{(1)''} p(e^{-i\alpha}\delta_{m,1} - e^{i\alpha}\delta_{m,-1})$ and, as a consequence the amplitudes a_m and b_m are zeros except $a_{\pm 1}$ and $b_{\pm 1}$, as expected from symmetry arguments. Once the amplitudes are determined, the scattered field, given by Eqs. (9) and (10) can be calculated at every point in the interior region (medium 1) and in the exterior region (medium 2). The total electromagnetic field allows us to calculate optical characteristics such as the power emitted and the power radiated by the dipole. The time average emitted power can be calculated from the integral of the normal component of the complex Poynting vector flux through an imaginary cylinder of length L and radius $\rho_0 < a$ that encloses the dipole (see Figure 1)

$$P = \rho_0 L \int_0^{2\pi} \text{Re} \left\{ \vec{S}(\rho_0, \phi) \cdot \hat{r} \right\} d\phi, \quad (22)$$

where

$$\vec{S}(\rho_0, \phi) = \frac{c}{8\pi} \left(-\frac{i}{k_0 \varepsilon_1} \right) \hat{z} \times \nabla_t [\varphi_i + \phi_s^{(1)}] \times \hat{z} [\varphi_i + \phi_s^{(1)}]^*. \quad (23)$$

Introducing Eq. (23) into Eq. (22), we obtain

$$P = \quad (24)$$

$$\frac{\rho_0 L c^2}{8\pi\omega\varepsilon_1} \int_0^{2\pi} \text{Re} \left\{ -i [\varphi_i + \varphi_s^{(1)}]^* \frac{\partial}{\partial \rho} [\varphi_i + \varphi_s^{(1)}] \right\} d\phi.$$

After some algebraic manipulation, the following results are found (see appendix)

$$P = \frac{\pi\omega^3 p^2}{4c^2} + \frac{\omega p}{4\sqrt{\varepsilon_1}} \times \text{Re} \left\{ i \sum_{m=-\infty}^{+\infty} J_m(k_1\rho') [a_{m+1} e^{i\alpha} + a_{m-1} e^{-i\alpha}] e^{im\phi'} \right\}. \quad (25)$$

Similarly, the time average radiative power emitted can be evaluated by calculating the complex Poynting vector flux through an imaginary cylinder of length L and radius $\rho_1 > a$ that encloses the graphene-coated cylinder (see Figure 1)

$$P_{sc} = \frac{\rho_1 L c^2}{8\pi\omega\varepsilon_2} \int_0^{2\pi} \text{Re} \left\{ -i [\varphi_s^{(2)}]^* \frac{\partial}{\partial \rho} [\varphi_s^{(2)}] \right\} d\phi, \quad (26)$$

In the far-field region the calculation of the scattered fields given by Eq. (10) can be greatly simplified using the asymptotic expansion of the Hankel function for large argument. After some algebraic manipulation, we obtain

$$P_{sc} = \frac{\rho_1 L c^2}{2\pi\omega\varepsilon_2} \sum_{m=-\infty}^{+\infty} |b_m|^2. \quad (27)$$

To characterize quantitatively the effect of the graphene coating, we define the normalized spontaneous emission rate F as the ratio between the power emitted by the dipole, given by Eq. (25), and the power emitted by the same dipole embedded in an unbounded medium 1. In a similar way, the radiative efficiency F_{sc} is defined as the ratio between the power radiated by the dipole, given by Eq. (27), and the power emitted by the dipole in the unbounded medium 1.

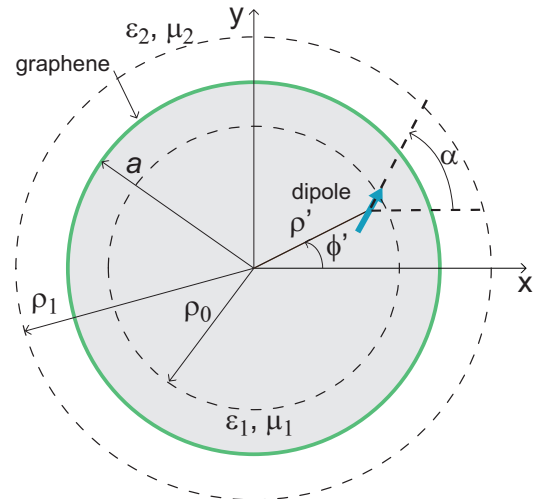


Figure 1. Schematic illustration of the system. An optical dipole emitter is inside a graphene-coated dielectric cylinder. The cylinder radius is a and the graphene surface conductivity is σ .

3. Results

We first briefly illustrate the emission and radiation characteristics in a dielectric wire without graphene coating (bare wire). Next, we consider a dielectric wire wrapped with a graphene coating. In all the examples the core (radius $a = 0.5\mu\text{m}$) is made of a transparent material ($\varepsilon_1 = 3.9$, $\mu_1 = 1$) and is embedded in vacuum

($\mu_2 = \varepsilon_2 = 1$). Rotational symmetry allows the emitter to be positioned on the \hat{x} axis ($\phi' = 0$).

3.1. Uncoated dielectric wire

In Figure 2a we plot the frequency dependence of the normalized spontaneous emission (per unit length) for an emitter localized at $\rho' = 0$, on the wire axis, and for $\rho' = 0.4\mu\text{m}$. The dipole moment \vec{p} is oriented in the radial direction ($\alpha = 0$). Due to the dielectric wire is lossless, the curve in this figure also represents the radiation decay rate efficiency of the emitter. The peaks on the curve for $\rho' = 0$ correspond to the first two Mie dipolar resonances and are associated with the complex poles at the zeros of the denominators D_1 of the coefficients a_1 and b_1 in Eqs. (13) and (14) with $\sigma = 0$. The condition $D_1 = 0$ generates a series $\omega_{(1,l)}$ of complex roots indexed l , whose real parts determine the resonant frequencies and the imaginary parts determine the quality factor Q of the resonances ($Q \approx 1/|\text{Im}\omega_{(m,l)}|$). By using a Newton Raphson method, we have obtained $\omega_{(1,1)}/c = (3.69523 - i0.60191)\mu\text{m}^{-1}$ and $(\omega/c)_{(1,2)} = (7.02453 - i0.57879)\mu\text{m}^{-1}$, whose real part is in very good agreement with the spectral position of the peaks. Consistent with causality, $\text{Im}\omega_{(m,l)}$ is strictly negative. The emission curve for $\rho' = 0.4\mu\text{m}$ shows the peaks corresponding to resonances whose eigenfrequencies are zeroes of the denominator D_m in Eqs. (13) and (14) with $\sigma = 0$ and with $1 \leq m \leq 6$ (see table 1). The values of the damping rates $|\text{Im}\omega_{(m,1)}|$ decrease with m , resulting in high Q resonances as frequency is increased. This fact is confirmed by the curve for $\rho' = 0.4\mu\text{m}$ in Figure 2a, since the width at half maximum of resonance peaks are decreasing with increasing frequency.

m	$\text{Re}\omega_{(m,l)}/c$	$ \text{Im}\omega_{(m,l)}/c $
1	1.37324	1.75516
2	3.73355	1.83205
3	5.69079	0.67741
4	6.86403	0.39975
5	8.09922	0.24052
6	9.33293	0.14277

Table 1. Resonance frequencies $\omega_{(m,l)}$ for the first six eigenmodes ($1 \leq m \leq 6$ and $l = 1$), $R = 0.5\mu\text{m}$, $\mu_c = 0.5\text{eV}$, $\gamma = 0.1\text{meV}$, $\varepsilon_1 = 3.9$, $\mu_1 = 1$, $\varepsilon_2 = 1$, $\mu_2 = 1$.

On the other hand, similar values between real parts of the dipolar $\omega_{(1,2)}/c$ and of the octupolar $\omega_{(4,1)}/c$ eigenfrequencies, suggest that these two resonances can be excited at the same emission frequency. This fact is showed in Figure 2a, where two peaks near $7\mu\text{m}^{-1}$, one on the curve for $\rho' = 0$ and the other one on the curve for $\rho' = 0.4\mu\text{m}$, are marked with a dot. The insets show the spatial

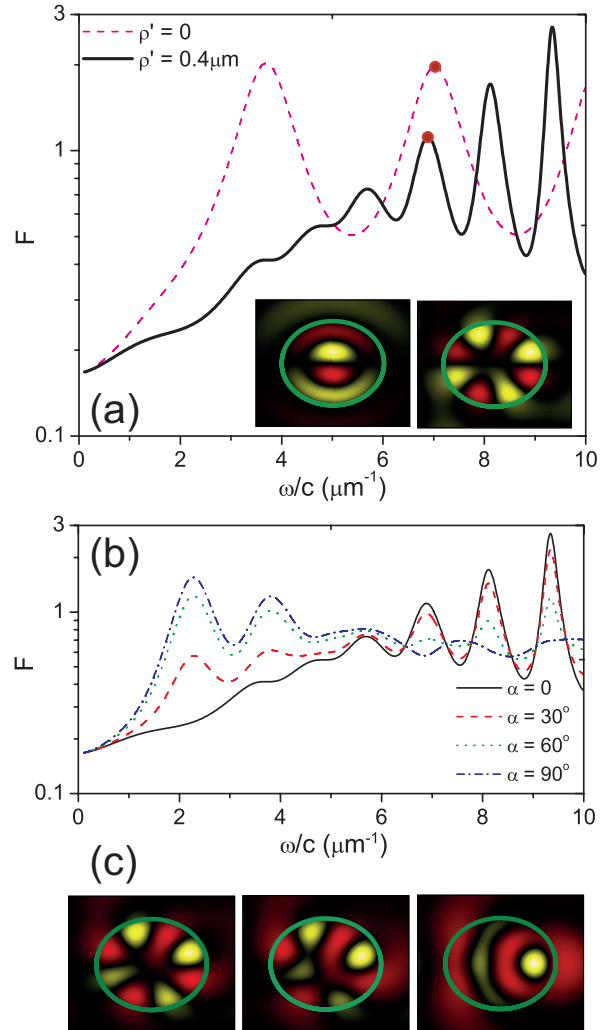


Figure 2. Spontaneous emission efficiency for a bare dielectric wire with a radius $a = 0.5\mu\text{m}$, constitutive parameters $\varepsilon_1 = 3.9$ and $\mu_1 = 1$ in a vacuum, calculated for $\alpha = 0^\circ$ (a), and for $\alpha = 0^\circ, 30^\circ, 60^\circ, 90^\circ$ (b). The insets in (a) show the magnetic field distributions $\varphi(\rho, \phi)$ near the wire for $\omega/c = 7\mu\text{m}^{-1}$. Red, negative values, yellow, positive values. (c) Near magnetic field distribution for the octupole resonance, $\alpha = 30^\circ, 60^\circ, 90^\circ$ and $\rho' = 0.4\mu\text{m}$.

distribution of the magnetic field $\varphi(\rho, \phi)$ calculated at the emission frequency $\omega/c = 7\mu\text{m}^{-1}$ for the case in which the emitter is localized at the wire center (left) and in case where the emitter is localized at $\rho' = 0.4\mu\text{m}$ (right). This result, is a clear confirmation that different resonances (dipolar and octupolar in this case) can be excited by moving the emitter from the wire center.

In Figure 2b the normalized spontaneous emission curves are depicted for different orientation angles $\alpha = 0, 30^\circ, 60^\circ$, and 90° when the source is placed at $\rho' = 0.4\mu\text{m}$. To illustrate the effects of varying the orientation angle α in the field near to the dielectric wire, in Figure 2c we have plotted the spatial

distribution of the magnetic field for the octupolar resonance and for $\alpha = 30^\circ, 60^\circ$ and 90° . We observe that these shapes are rotated and highly distorted with respect the shape calculated for $\alpha = 0$ showed in the inset of Figure 2a.

3.2. Graphene-coated wire

Having studied bare dielectric wires, we next explore the effects that a graphene coating has on the emission and the radiation spectrum of a dipole emitter localized inside the wire. In particular, the coating is expected to introduce LSPs mechanisms, which were absent in the bare wire, which are able to enhance the emission properties at resonance frequencies. The dashed and solid curves in Figure 3 display the frequency dependence of the spontaneous emission and the radiation efficiencies for the same wire considered in the previous example but now it is wrapped with a graphene coating. We used Kubo parameters $\mu_c = 0.5\text{eV}$, $\gamma = 0.1\text{meV}$, $T = 300\text{K}$, emission frequencies in the range between $0.1\mu\text{m}^{-1}$ (5 THz or wavelength $\lambda = 60\mu\text{m}$) and $6\mu\text{m}^{-1}$ (30 THz or wavelength $\lambda = 10\mu\text{m}$), and for three different locations of the dipole, $\rho' = 0, 0.1\mu\text{m}$, and $0.4\mu\text{m}$. Figure 3a shows that both F and F_{sc} efficiencies are enhanced at a frequency near $0.17\mu\text{m}^{-1}$ ($\lambda = 36.35\mu\text{m}$) corresponding to the dipolar plasmon resonance of the graphene-coated wire. The correspondence between the spectral position of these peaks and the dipolar plasmon resonance can be clearly seen by calculating the complex root ω_1/c of the common denominator $D_1(\omega)$ in equations (13) and (14). We have obtained $\omega_1/c = (0.17287 - 4.57289 \cdot 10^{-4})\mu\text{m}^{-1}$ whose real part is in very good agreement with the spectral position of the peaks. In contrast to bare wires, where the emission decay rate reaches values close to unity at multipolar resonances, we obtain enhancement factors in both the emission and radiation decay rate efficiencies of around five orders of magnitude when the wire is wrapped with a graphene coating. Furthermore, we find that high-order plasmon resonances are excited when the emitter is moved from the wire center, as can be seen in Figure 3b where the curves of F and F_{sc} have been plotted for $\rho' = 0.1\mu\text{m}$. In addition to the maximum enhancement in both the emission and the radiation spectra at a frequency near $0.17\mu\text{m}^{-1}$ ($m = 1$ or dipolar resonance), a local maximum enhancement near $0.24\mu\text{m}^{-1}$ corresponding to the quadrupolar plasmon resonance ($m = 2$) appear. Other local maxima, particularly noticeable in the emission spectra, occur at frequencies near $0.30\mu\text{m}^{-1}$ ($m = 3$ or hexapolar resonance) and $0.35\mu\text{m}^{-1}$ ($m = 4$ or octupolar resonance). By calculating the complex root ω_m of the common denominator $D_m(\omega)$ in equations (13) and (14), we

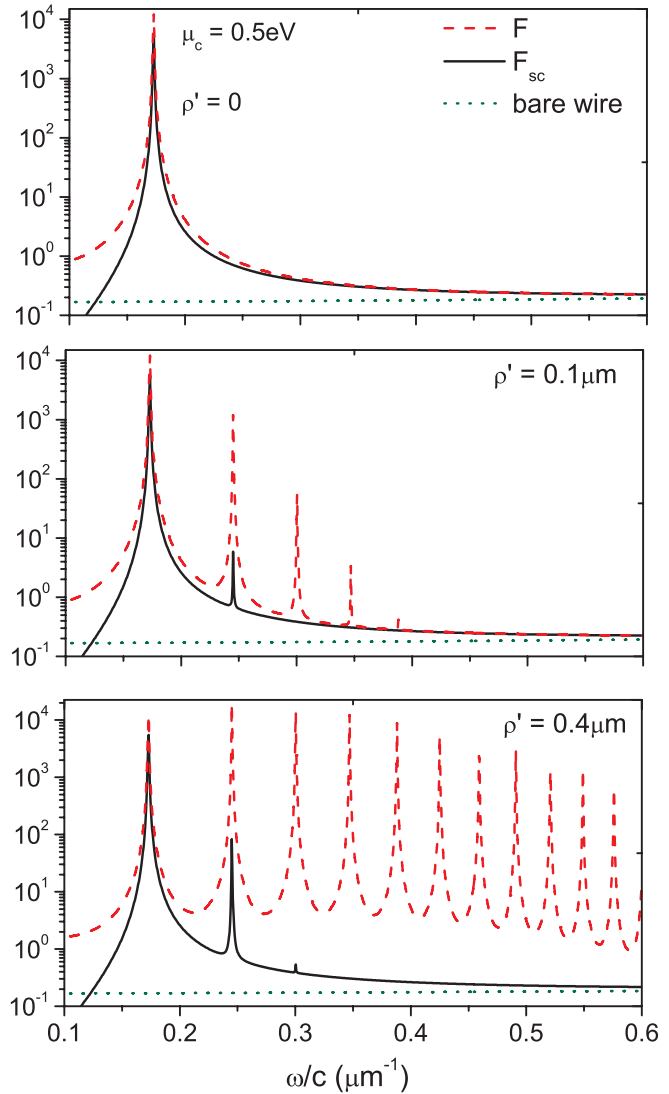


Figure 3. Efficiency (per unit length) curves, calculated for $\mu = 0.5\text{eV}$, $T = 300\text{K}$, $\gamma_c = 0.1\text{meV}$, $\varepsilon_1 = 3.9$, $\mu_1 = 1$ and $\varepsilon_2 = 1$, $\mu_2 = 1$. The emission efficiency curve corresponding to the uncoated cylinder is given as a reference. The emitter is localized at $\rho' = 0$ (a), $\rho' = 0.1\mu\text{m}$ (b), $\rho' = 0.4\mu\text{m}$ (c), with its dipole moment oriented in the $+\hat{x}$ direction ($\alpha = 0$).

have obtained $\omega_2/c = (0.24509 - 2.53123 \cdot 10^{-4})\mu\text{m}^{-1}$, $\omega_3/c = (0.30038 - 2.52376 \cdot 10^{-4})\mu\text{m}^{-1}$ and $\omega_4/c = (0.34697 - 2.52553 \cdot 10^{-4})\mu\text{m}^{-1}$ for which their real parts are in very good agreement with the spectral position of the peaks. When ρ' is increased, the enhancement factors in the spontaneous emission curve at frequencies corresponding to high-order resonances becomes more and more pronounced. This fact can be viewed in figure 3c in which the emission efficiencies for $m = 1, 2, 3$ and 4 reach similar values ($\approx 10^4$).

It is worth noting that the width at half maximum of the resonance peaks in Figure 3c, *i.e.*, the quality factor of the resonance Q , almost not shows any significant dependence on the position of the peak.

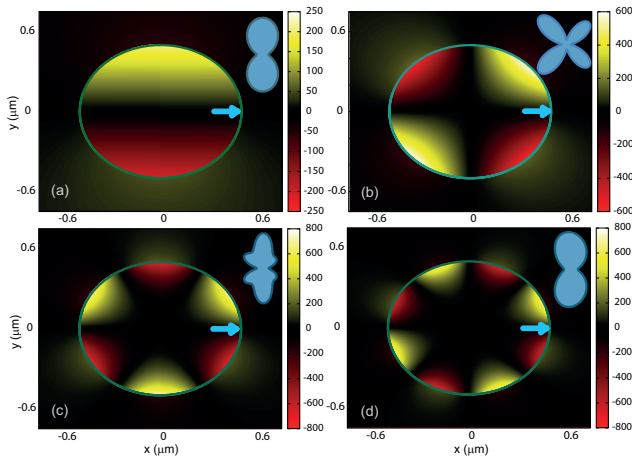


Figure 4. Map of the magnetic field $\varphi(\rho, \phi)$ at a fixed time for plasmon resonances of the wire considered in Figure 3. Red, negative values, yellow, positive values. The frequency emission is $\omega/c = 0.17287\mu\text{m}^{-1}$ (a), $\omega/c = 0.24509\mu\text{m}^{-1}$ (b), $\omega/c = 0.30038\mu\text{m}^{-1}$ (c), and $\omega/c = 0.34697\mu\text{m}^{-1}$ (d). The dipole emitter is indicated with an arrow. All parameters are the same as in Figure 3c.

This agree well with the fact that the damping rate take the value $\text{Im}\omega_m/c \approx \gamma/2 = 2.5 \cdot 10^{-4}\mu\text{m}^{-1}$ for large enough m values [32]. Although the enhancement factors in the radiation curve are less noticeable than those in the emission curve, these peaks are increased when ρ' is increased, as can be seen by comparing the radiation curves in Figures 3b and 3c. Moreover, we observe that a peak at a frequency near $0.30\mu\text{m}$ (in which hexapolar order resonance occur), absent in the curve corresponding to $\rho' = 0.1\mu\text{m}$, becomes just visible.

In Figure 4 we plot the spatial distribution of the near magnetic field $\varphi(\rho, \phi)$ for the wire considered in Figure 3 and for the first four plasmon resonances. We have considered the particular case of the emitter localized at $\rho' = 0.4\mu\text{m}$ as in Figure 3c. The emission frequencies are $\omega/c = 0.17287\mu\text{m}^{-1}$ (Figure 4a), $\omega/c = 0.24509\mu\text{m}^{-1}$ (Figure 4b), $0.30038\mu\text{m}^{-1}$ (Figure 4c), and $0.34697\mu\text{m}^{-1}$ (Figure 4d), *i.e.*, the values corresponding to the real part of the complex poles $\omega_{(m,1)}/c$ of the multipole coefficients a_m and b_m ($m = 1, 2, 3,$ and 4) and for which the strongest maxima in the emission efficiency occur. At these frequencies, the near field distributions follow the typical dipolar, quadrupolar, hexapolar and octupolar patterns. Contrary to what happens in bare wires, the presence of a surface current density $j_\phi = \frac{4\pi\sigma}{c}E_\phi$ induced on the graphene coating and the boundary condition in Eq. (12) lead to a discontinuity at $\rho = a = 0.5\mu\text{m}$ as can be observed in Fig. 4. For example, the map of the magnetic field showed in Figure 4c

is characterized by six zones, three of them are red inside the cylinder and are yellow outside the cylinder, pointing out that the magnetic field changes from negative values to positive values when passing from inside to outside of the cylinder. In the other three zones, yellow inside the cylinder and red outside the cylinder, the magnetic field changes from positive to negative values when passing from inside to outside of the cylinder.

As well as the near field maps at resonance frequencies are closely related with the amplitude and location of the maxima in the emission spectra, the far field maps are related with the peak characteristics in the radiation spectra. The inset in Figure 4a shows that, for the emission frequency $\omega/c = 0.17287\mu\text{m}^{-1}$ ($\omega/c = \text{Re}\omega_1/c$), the far field intensities, namely $dP_{sc}/d\phi$ which is the fraction of the emitted power that is scattered into the angular region about the scattering direction ϕ , are dominated by an dipole pattern. The integral of $dP_{sc}/d\phi$ over all angles, *i.e.*, the radiative decay rate, is found to be 10^4 times larger than that of the same dipole emitter in the absence of the graphene-coated wire, as can be seen in Figure 3c. When the emission frequency is $0.24509\mu\text{m}^{-1}$ ($\omega/c = \text{Re}\omega_2/c$), the radiation efficiency showed in Figure 3c exhibits a strong enhancement (an enhancement factor near three orders of magnitude greater than that of the same emitter in the absence of the graphene-coated wire) and the far field intensities are dominated by an electromagnetic quadrupole pattern, as indicated in the inset in figure 4b. Similarly, when the emission frequency is $0.30038\mu\text{m}^{-1}$ ($\omega/c = \text{Re}\omega_3/c$), the radiation efficiency plotted in Figure 3c exhibits a very weak peak, and as a result, a small hexapolar pattern overlaps the dipole pattern in the far-field intensities, as indicated in the inset in figure 4c. On the other hand, no peak is observed in the radiation efficiency curve when the emission frequency is $0.34697\mu\text{m}^{-1}$ ($\omega/c = \text{Re}\omega_4/c$). At this frequency, the far-field intensities are dominated by an electromagnetic dipole, as indicated in the inset in Figure 4d.

Contrary to the case of bare wires, where both the emission and radiation efficiencies are highly modified when the dipole is rotated, in the graphene coated dielectric wire we have observed that neither F nor F_{sc} efficiencies show a noticeable dependence on the orientation angle α . However, the shape of the near field distribution and of the far field intensities strongly depend on α . This fact can be seen in Figure 5, where we have plotted the near field and the power patterns for four dipole orientations: $\alpha = 0, 30^\circ, 60^\circ$ and 90° , at a specifically frequency corresponding to the quadrupolar plasmon resonance. When the dipole is rotated, both the near field map

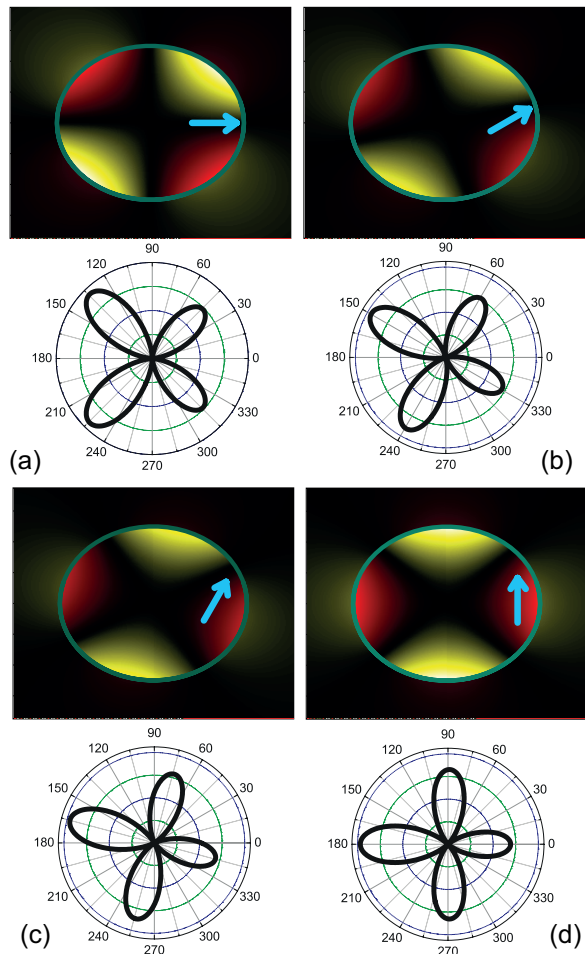


Figure 5. Map of the near magnetic field $\varphi(\rho, \phi)$ and the far field intensities at a fixed time for the quadrupolar plasmon resonance of the wire and for $\alpha = 0$ (a), $\alpha = 30^\circ$ (b), $\alpha = 60^\circ$, $\alpha = 90^\circ$ (d). Red, negative values, yellow, positive values. The frequency emission is $\omega/c = 0.24509\mu\text{m}^{-1}$ and the emitter is localized at $\rho' = 0.4\mu\text{m}$, $\phi' = 0$. The dipole emitter is indicated with an arrow. All other parameters are the same as in Figure 4b.

and the far field intensities are rotated with respect the $\alpha = 0$ case. Unlike the case of bare wires, where the near field distortion due to the rotation of the source is remarkable (see Figure 2c), Figure 5 shows that when the dielectric wire is wrapped with a graphene coating only a rotation of the near field is appreciable, being its distortion negligible. On the other hand, as α is increased, the shape of the far field intensities are more and more distorted until arriving at the shape shown in Figure 5d corresponding to $\alpha = 90^\circ$. Same behavior has been observed [not shown in Figure 5] at the other plasmon resonance frequencies.

To examine the effects of the emitter localization on plasmon resonances, Figure 6 shows the emission and the radiation decay rates as a function of the distance to the wire center. The emission frequency is chosen such that the emission is resonant at the

orders: dipolar (a), quadrupolar (b), hexapolar (c) and octupolar (d). At distance $0\mu\text{m}$, the emission and the radiation decay rates for the dipole resonance are both 10^4 times larger than in the absence of the graphene-coated cylinder. When ρ' is increased from this value, both efficiency curves decrease to reach their lowest value at $\rho' = a = 0.5\mu\text{m}$ as its shown in Figure 6a. In contrast, for the quadrupole resonance, Figure 6b shows that both efficiency curves take a value close to unity at $\rho' = 0\mu\text{m}$ and that these curves increase with the increasing of ρ' . The same behavior is observed in Figure 6c for the hexapole resonance, although the maximum value in the radiative decay efficiency is much lower than the maximum value in the quadrupolar resonance curve. For the octupole resonance, the value of the radiative decay efficiency does not shows any significant dependence on the position of the emitter, as can be seen in Figure 6d.

4. Conclusions

In conclusion, we have presented an analytical classical method based on the separation of variables approach to find the emission and radiation characteristics of an optical emitter inside a circular cross-section wire coated with a graphene layer. The method has been used to investigate how the location of the emitter, as well as the orientation of its dipole moment, affect the power emitted by the source. We found that the interplay between the optical emitter and the LSPs in the graphene coating strongly influences the spontaneous decay rate as well as the radiation characteristics. We have compared the results with those obtained for the same dielectric wire but without a graphene layer (bare wire), in which the decay rates are enhanced at resonances associated with cavity modes.

As might be expected from symmetry arguments, for the optical emitter placed on the wire center, we found that both the emission and radiation decay rates are enhanced just at dipolar resonance frequency. Instead, an enhancement at frequency of high-order resonances appear when the emitter is moved from the axis of the wire. The correspondence between the position of the spectral peaks and the multipolar resonances (cavity or plasmonic) has been clearly shown by calculating the complex poles of the coefficients of the multipole expansion of the electromagnetic field. In case of bare wires, cavity effects are intensified as frequency increases, *i.e.*, where high Q resonances take place. On the contrary, for graphene coated wire, the resonance damping rate take the quasistatic value $\text{Im}\omega_m \approx \gamma/2$ for large enough m values. As a consequence, the resonance Q factor shows any dependence on the position of the spectral

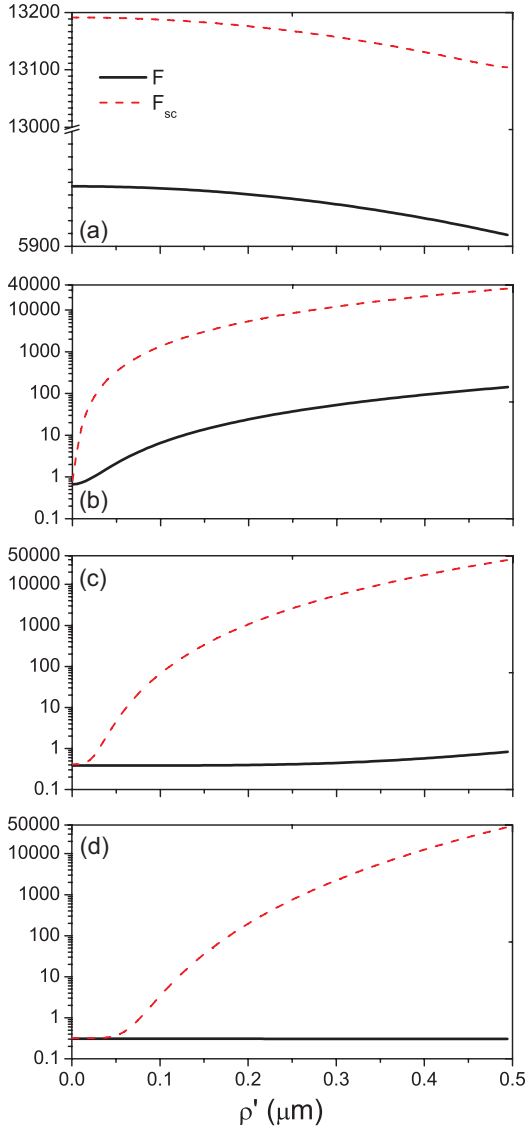


Figure 6. Emission and radiation decay efficiencies (per unit length) as a function of the distance from the wire center for the dipole (a), the quadrupole (b), the hexapole (c) and the octupole (d) resonance frequencies. All other the parameters are the same as in Figure 3. The emitter is located on the \hat{x} axis with its dipole moment oriented in the radial direction ($\alpha = 0$).

peaks. Moreover, whereas the emission and radiation decay rates are highly modified with the orientation of the dipole emitter in case of bare wires, we have found that neither emission nor radiation decay rates show a noticeable dependence on the orientation angle in case of graphene coated wires.

The spatial distribution of the electromagnetic field near the wire for different resonance frequencies and positions of the emitter have been investigated. The multipolar order revealed by the topology of the near field agrees well with the multipolar order revealed by the spectral position of the emission decay rate peak. We have shown the modifications in the near

field distribution by varying the orientation of the dipole.

Acknowledgment

The author acknowledge the financial support of Consejo Nacional de Investigaciones Científicas y Técnicas, (CONICET, PIP 451).

5. Appendix I

In an unbounded medium (constitutive parameters ε , μ) the vector potential $A(\vec{\rho}, \phi)$ satisfy the inhomogeneous Helmholtz equation [33]

$$\nabla^2 \vec{A} + k^2 \vec{A} = 4\pi i k_0 \vec{p} \frac{1}{\rho} \delta(\rho - \rho') \delta(\phi - \phi') \quad (28)$$

where ρ' and ϕ' denotes the position of the line dipole source, with $\rho' < a$, $k^2 = \varepsilon \mu k_0^2$ and $\vec{A} = A_\rho \hat{r} + A_\phi \hat{\phi}$. Since

$$\delta(\phi - \phi') = \frac{1}{2\pi} \sum_{-\infty}^{+\infty} e^{im(\phi - \phi')}, \quad (29)$$

we can write

$$A_\tau(\rho, \phi, \rho', \phi') = \sum_{m=-\infty}^{+\infty} a_{\tau,m}(\rho, \rho') e^{im(\phi - \phi')}, \quad (30)$$

where the subscript τ denotes ρ or ϕ . To determine $a_{\tau,m}(\rho, \rho')$, we insert expressions (29) and (30) into Eq. (28) and obtain

$$\left[\frac{d}{d\rho} \left(\rho \frac{d}{d\rho} \right) - \frac{m^2}{\rho} + k^2 \rho \right] a_{\tau,m}(\rho, \rho') = 2ik_0 p_\tau \delta(\rho - \rho'). \quad (31)$$

Taking into account the finiteness at the origin and the radially outgoing property, we obtain

$$a_{\tau,m}(\rho, \rho') = A J_m(k\rho_{<}) H_m^{(1)}(k\rho_{>}), \quad (32)$$

where $\rho_{<}$ ($\rho_{>}$) is the smaller (larger) of ρ and ρ' . The coefficient A is determined by the condition

$$\rho \frac{da_{\tau,m}}{d\rho} \Big|_{\rho_+} - \rho' \frac{da_{\tau,m}}{d\rho} \Big|_{\rho_-} = \frac{2ik_0 p_\tau}{\rho'}. \quad (33)$$

By using $W(J_m(x), H_m^{(1)}(x)) = 2i/\pi x$ where W denotes the Wronskian, we obtain $A = \pi k_0 p_\tau$. Finally,

$$A_\tau(\rho, \phi, \rho', \phi') = \sum_{m=-\infty}^{+\infty} \pi k_0 p_\tau J_m(k\rho_{<}) H_m^{(1)}(k\rho_{>}) \times e^{im(\phi - \phi')}. \quad (34)$$

6. Appendix II

Here, we derive an analytical expression for the first term in Eq. (24), *i.e.*, the contribution of the primary field emitted by the dipole. It is given by

$$P_i = \frac{\rho_0 L c^2}{8\pi\omega\epsilon_1} \int_0^{2\pi} \text{Re} \left\{ -i\varphi_i^* \frac{\partial}{\partial\rho} \varphi_i \right\} d\phi \quad (35)$$

Introducing Eq. (8) into Eq. (35) we obtain

$$\begin{aligned} & \text{Re} \left\{ \frac{-i\pi k_0^3 k_1 L \rho_0}{8} \sum_{m,n} J_m(x') J_n(x')^* \right. \\ & \times \int_0^{2\pi} [H_m^{(1)}(x)'' H_n^{(1)}(x)'^* |p_\phi|^2 \\ & - im \frac{d}{dx} \left(\frac{H_m^{(1)}(x)}{x} \right) H_n^{(1)}(x)'^* p_\rho p_\phi^* \\ & + in H_m^{(1)}(x)'' \frac{H_m^{(1)}(x)^*}{x} p_\phi p_\rho^* \\ & \left. + mn \frac{d}{dx} \left(\frac{H_m^{(1)}(x)}{x} \right) \frac{H_m^{(1)}(x)^*}{x} |p_\rho|^2 \right] \\ & \times e^{i(m-n)(\phi-\phi')} d\phi \}, \end{aligned} \quad (36)$$

where $x = k_1 \rho_0$ and $x' = k_1 \rho'$. Taking into account the recurrence relations of the Hankel function [34], $p_\rho = p \sin(\alpha - \phi)$ and $p_\phi = p \cos(\alpha - \phi)$, we can write Eq. (35) as

$$\begin{aligned} P_i &= \frac{c\pi k_0^3 L p^2}{4} \sum_{m=-\infty}^{+\infty} \{ [J_m(x')]^2 \\ & + J_m(x') J_{m+2}(x') \cos(2[\phi' - \alpha]) \} = \frac{c\pi k_0^3 L p^2}{4} \end{aligned} \quad (37)$$

where we have used $W(J_m(x), Y_m(x)) = 2/\pi x$, $[J_0(x)]^2 + 2 \sum_{k=1}^{+\infty} [J_k(x)]^2 = 1$ and $-J_1(x)^2 + 2 \sum_{k=0}^{+\infty} J_k(x) J_{k+2}(x) = 0$ [34].

It is worth noting that the same result can be obtained by using the Poynting theorem [16],

$$P_i = \frac{\omega}{2} \text{Im} \left\{ \vec{p} \cdot \vec{E}_i(\vec{x}') \right\} \quad (38)$$

where the field $\vec{E}_i(\vec{x}')$ is the primary electric dipole field evaluated at the dipole position \vec{x}' .

References

- [1] H. Raether 1988 *Surface Plasmons On Smooth And Rough Surfaces And On Gratings* (Berlin: Springer-Verlag)
- [2] Maier S A 2007 *Plasmonics: Fundamentals and Applications* (New York: Springer)
- [3] Fengnian Xia, Comment on Graphene versus metal plasmons, *Nature Photonics* 7, 420 (2013).
- [4] Jablan J., Soljacic M., Buljan H. 2013 Plasmons in graphene: fundamental properties and potential applications *Proc. IEEE* 101 1689–1704
- [5] S.H. Song, S.H. Jang, J. Chung, S.H. Jin, B.H. Kim, S.H. Hur, S. Yoo, Y.-H. Cho, S. Jeon Highly efficient light-emitting diode of graphene quantum dots fabricated from graphite intercalation compounds *Adv. Opt. Mater.*, 2 (2014), pp. 1016–1023
- [6] María C. Dalfovo, Gabriela I. Lacconi, Moónica Moreno, Marta C. Yappert, Gamini U. Sumanasekera, Roberto C. Salvezza, and Francisco J. Ibanez, Synergy between Graphene and Au Nanoparticles (Heterojunction) towards Quenching, Improving Raman Signal, and UV Light Sensing, *Acs Appl. Mater. Interfaces*, 6 (2014), pp 6384–8391
- [7] Francesco Bonaccorso, Luigi Colombo, Guihua Yu, Meryl Stoller, Valentina Tozzini, Andrea C. Ferrari, Rodney S. Ruoff, Vittorio Pellegrini, Graphene, related two-dimensional crystals, and hybrid systems for energy conversion and storage, *Science* 347, (6217) (2015).
- [8] Tame M S, McEney K R, Ozdemir K, Lee J, Maier S A and Kim M S 2013 Quantum plasmonics *Nature Physics* 9 329–40
- [9] Christensen T, Jauho A-P, Wubs M and Mortensen N 2015 Localized plasmons in graphene-coated nanospheres *Phys. Rev. B* 91 125414
- [10] Hanson G W, Forati E, Linz W, Yakovlev A B 2012 Excitation of terahertz surface plasmons on graphene surfaces by an elementary dipole and quantum emitter: strong electrodynamic effect of dielectric support *Phys. Rev. B* 86 235440
- [11] Huidobro P A, Nikitin A Y, González-Ballesteros C, Martín-Moreno L, and García-Vidal F J 2012 Superradiance mediated by graphene surface plasmons *Phys. Rev. B* 85 155438
- [12] Kort-Kamp W J M, Amorim B, Bastos G, Pinheiro F A, Rosa F S S, Peres N M R, and Farina C 2015 Active magneto-optical control of spontaneous emission in graphene *Phys. Rev. B* 92 205415
- [13] Karanikolas V D, Marocico C A, and Bradley A L 2015 Effect of surface-plasmon polaritons on spontaneous emission and intermolecular energy-transfer rates in multilayered geometries *Phys. Rev. B* 91 125422
- [14] Koppens F H L, Chang D E and García de Abajo F J 2011 Graphene plasmonics: A platform for strong light-matter interactions *Nano Lett.* 11 3370–77
- [15] Zhang L, Fu X, Zhang M, and Yang J 2013 Spontaneous emission in paired graphene plasmonic waveguide structures *Optic Express* 21 7897–907
- [16] Mauro Cuevas, Surface plasmon enhancement of spontaneous emission in graphene waveguides, *Journal of Optics* 18, 105003 (2016)
- [17] D. P. Fussell, R. C. McPhedran, and C. Martijn de Sterke, Decay rate and level shift in a circular dielectric waveguide, *Phys. Rev. A* 71, 013815 (2005).
- [18] Julien Barthes, Alexandre Bouhelier, Alain Dereux and Gerard Colas des Francs, Coupling of a dipolar emitter into one-dimensional surface plasmon, *Scientific Reports* 3, 2734, (2013).
- [19] Vasilios Karanikolas, Cristian A. Marocico, and A. Louise Bradley, Spontaneous emission and energy transfer rates near a coated metallic cylinder, *Phys. Rev. A* 89, 063817 (2014).
- [20] Luis Martín-Moreno, F. Javier García de Abajo, and Francisco J. García-Vidal, Ultraefficient Coupling of a Quantum Emitter to the Tunable Guided Plasmons of a Carbon Nanotube, *Phys. Rev. Lett.* 115, 173601 (2015).
- [21] David Dzsotjan, Anders S. Sorensen, and Michael Fleischhauer, Quantum emitters coupled to surface plasmons of a nanowire: A Green's function approach, *Phys. Rev. B* 82, 075427 (2010).
- [22] A. V. Akimov, A. Mukherjee, C. L. Yu, D. E. Chang, A. S. Zibrov, P. R. Hemmer, H. Park and M. D. Lukin, Generation of single optical plasmons in metallic nanowires coupled to quantum dots, *Nature* 450, 402–406 (2007).
- [23] L. Rogobete, C. Henkel, Spontaneous emission in a subwavelength environment characterized by boundary

- integral equations, *Phys. Rev.* 70, 063815 (2004).
- [24] Lavinia Rogobete, Hannes Schniepp, Vahid Sandoghdar, Carsten Henkel, Spontaneous emission in nanoscopic dielectric particles, *Optics Letters* 28, (2003).
- [25] S P Feofilov, A B Kulinkin, D A Eurov, D A Kurdyukov and V G Golubev, Fluorescence spectroscopy study of mesoporous SiO₂ particles containing Gd₂O₃:Eu³⁺, *Materials Research Express* 1 (2014) 025019
- [26] G. H. Jeong, A. A. Farajian, R. Hatakeyama, T. Hirata, T. Yaguchi, K. Tohji, H. Mizuseki, and Y. Kawazoe, Cesium encapsulation in single-walled carbon nanotubes via plasma ion irradiation: Application to junction formation and ab initio investigation, *Phys. Rev. B* 68, 075410 (2003).
- [27] He X, Zhang X, Zhang H and Xu M 2014 Graphene covered on microfiber exhibiting polarization and polarizationdependent saturable absorption *IEEE J. Sel. Top. Quantum Electron.* 20 4500107
- [28] Vahid Siahpoush, Thomas Sondergaard, and Jesper Jung, Green's function approach to investigate the excitation of surface plasmon polaritons in a nanometer-thin metal film, *Phys. Rev. B* 85, 075305 (2012).
- [29] Falkovsky F A 2008 Optical properties of graphene and IV–VI semiconductors. *Phys Usp* 51 887–97
- [30] Milkhailov S A and Siegler K 2007 New electromagnetic mode in graphene *Phys Rev Lett* 99 016803
- [31] Riso M, Cuevas M and Depine R A 2015 Tunable plasmonic enhancement of light scattering and absorption in graphenecoated subwavelength wires *Journal of Optics* 17 075001
- [32] M Cuevas , M Riso, and R A Depine 2016 Complex frequencies and field distributions of localized surface plasmon modes in graphene-coated subwavelength wires *Journal of Quantitative Spectroscopy and Radiative Transfer* 173 26–33
- [33] Novotny L, and Hecht B *Principles of Nano-Optics*; Cambridge University Press: New York, 2006.
- [34] Abramowitz M. and Stegun I. A., *Handbook of Mathematical Functions* (New York: Dover) (1965)